Circular Dichroism and Magnetic Circular Dichroism Studies of the Active Site of p53R2 from Human and Mouse: Iron Binding and Nature of the Biferrous Site Relative to Other Ribonucleotide Reductases†

Pin-pin Wei,‡ Ane B. Tomter,§ Åsmund K. Røhr,§ K. Kristoffer Andersson,*,§ and Edward I. Solomon*,‡

Department of Chemistry, Stanford University, Stanford, California 94305, and Department of Molecular Biosciences, University of Oslo, P.O. Box 1041, Blindern, 0316 Oslo, Norway

Received June 6, 2006; Revised Manuscript Received September 11, 2006

ABSTRACT: Ribonucleotide reductases (RNR) catalyze the rate-limiting step in the synthesis of deoxyribonucleotides from the corresponding ribonucleotides in the synthesis of DNA. Class I RNR has two subunits: R1 with the substrate binding and active site and R2 with a stable tyrosyl radical and diiron cluster. Biferrous R2 reacts with oxygen to form the tyrosyl radical needed for enzymatic activity. A novel R2 form, p53R2, is a 351-amino acid protein induced by the "tumor suppressor gene" p53. p53R2 has been studied using a combination of circular dichroism, magnetic circular dichroism, variable-temperature variable-field MCD, and EPR spectroscopies. The active site of biferrous p53R2 in both the human (hp53R2) and mouse (mp53R2) forms is found to have one five-coordinate and one four-coordinate iron, which are weakly antiferromagnetically coupled through μ-1,3-carboxylate bridges. These spectroscopic data are very similar to those of *Escherichia coli* R2, and mouse R2, with a stronger resemblance to data of the former. Titrations of apo-hp53R2 and apo-mp53R2 with Fe(II) were pursued for the purpose of comparing their metal binding affinities to those of other R2s. Both p53R2s were found to have a high affinity for Fe(II), which is different from that of mouse R2 and may reflect differences in the regulation of enzymatic activity, as p53R2 is mainly triggered during DNA repair. The difference in ferrous affinity between mammalian R2 and p53R2 suggests the possibility of specific inhibition of DNA precursor synthesis during cell division.

Ribonucleotide reductases (RNRs)[1] catalyze the rate-limiting step in the synthesis of deoxyribonucleotides from the corresponding ribonucleotides in the synthesis of DNA (*1*−*3*). There are three classes of RNR, but the most prevalent is the oxygen-dependent class I RNR, which is found in all eukaryotes and *Escherichia coli* (*4*). This class contains a complex of two homodimeric proteins, R1 and R2. R2 contains a binuclear iron center and a stable tyrosyl radical required for the reduction of nucleotides (*5*−*10*). The tyrosyl radical is generated by the reaction of the reduced biferrous active site with dioxygen (*5*−*10*). Class I RNR is further divided into two subclasses, class Ia and Ib (*9*, *11*−*13*), and recently, a new subclass (Ic) has been proposed (*14*).

E. coli R2 and mouse R2 (mR2) have been characterized by spectroscopy and crystallography (*13*, *15*−*19*). The level of overall amino acid sequence identity between the *E. coli* R2 and mR2 is ∼25% (*20*). The higher level of sequence identity of mR2 with human R2 (98% homologous) makes it a better model for investigating the chemistry of human R2. However, *E. coli* R2 is the most well characterized member of the class Ia R2 family. Several crystal structures of the reduced binuclear iron site of *E. coli* R2 have been solved (*21*−*23*), and the spectroscopically supported crystal structure of the biferrous site has been determined to contain a four- and five-coordinate (4C,5C) Fe_2(II) center with two μ-1,3-carboxylate bridges (*16*−*18*). The recently determined crystal structure of the biferrous site of mR2 is similar to that of *E. coli* R2, but mR2 was noted to have a more open coordination site since an acetate at pH 6 can bind to one of the irons (*24*).

Recently, p53R2, a 351-amino acid p53-inducible protein that is strikingly similar to mammalian R2, has been isolated (*25*, *26*). The *p53*gene was discovered in 1979 (*27*−*30*) and is well-known as the "tumor suppressor gene" as it is inactivated more frequently than any other gene in a wide range of human cancers (*27*−*30*). In its normal state, *p53* exerts a tumor suppressing function by regulating cell-cycle arrest or by inducing apoptosis. The biological role of the p53R2 protein is significant as transgenic mice without the p53R2 gene can only live 8−14 weeks (*31*, *32*).

† Financial support for this research by NSF Biophysics Program Grant MCB-0342807 (E.I.S.), the Norwegian Cancer Society (K.K.A.), and a Fulbright grant (K.K.A.).

* To whom correspondence should be addressed. K.K.A.: phone, X-(47) 2285-6625; fax, X-(47) 2285-6041; e-mail, k.k.andersson@imbv.uio.no. E.I.S.: phone, (650) 723-4694; fax, (650) 725-0259; e-mail, edward.Solomon@stanford.edu.

‡ Stanford University.

§ University of Oslo.

[1] Abbreviations: RNR, ribonucleotide reductase; R2, subunit of ribonucleotide reductase; mR2, mouse R2 protein; hp53R2, p53-inducible isoform of R2 in humans; mp53R2, p53-inducible isoform of R2 in mice; EPR, electron paramagnetic resonance; CD, circular dichroism; MCD, magnetic circular dichroism; VTVH MCD, variable-temperature variable-field magnetic circular dichroism; 6C, 6 coordinate; 5C, 5 coordinate; 4C, 4 coordinate; SOC, spin orbit coupling; ZFS, zero-field splitting.

10.1021/bi061127p CCC: $33.50
Published on Web 11/03/2006

p53R2 is different from normal RNR R2s because it is induced in response to DNA damage, whereas normal R2 is only active during mitosis (*25*, *33*−*37*). The function of p53R2 is so critical that it can also be induced by alternative pathways in cells carrying a defective p53 gene (*38*). In addition, it has been shown that p53R2 can form a complex with R1 to supply cells with deoxyribonucleotides for DNA repair (*25*, *26*). p53R2 is thought to interact with the R1 subunit of mouse RNR which has been suggested to occur in an active hexameric form (*39*−*42*). The formation of a complex between R1 and R2 is vital, as the tyrosyl radical produced in R2 must be transferred to the active site of R1 for successful reduction of ribonucleotides (*6*−*9*, *43*, *44*). An iron−tyrosyl free radical center in active human p53R2 (hp53R2), which is analogous to mammalian R2, has been observed and confirms that p53R2 reacts with O_2 to generate a tyrosine radical (*26*). Tyrosyl radicals are essential for the initiation of the nucleotide reduction process that take place at the active site in R1. Human and mouse p53R2 (mammalian) are 80% homologous to mR2 and 30% homologous to *E. coli* R2, but the residues involved in the active site of hp53R2, as well as the metal ligation and tyrosine radical site, are conserved (*25*, *26*). Although crystal structures of p53 have been determined, there is no crystal structure available for hp53R2.

This study utilizes near-IR CD and MCD spectroscopy to probe the coordination environment of the $Fe(II)_2$ center in reduced human and mouse p53R2. VTVH MCD data were also collected to define the ground state as well as to examine the exchange interactions between the irons in the binuclear site which reflects the nature of the bridging ligands (*45*). Electron paramagnetic resonance (EPR) studies of reduced mouse and human p53R2 were carried out in an effort to examine the ground spin state. Titrations were performed to gain insight into the binding affinity and iron loading features of p53R2. Examination of the geometric and electronic structure of this site and comparison of these data with the library of R2 and binuclear iron protein data obtained in our labs allow insight into the relation of p53R2 to other biferrous ribonucleotide reductases.

EXPERIMENTAL PROCEDURES

Sample Preparation. Materials used for sample preparation were purchased from the following companies: Sigma (Hepes buffer, sodium chloride), Mallinckroft (ferrous ammonium sulfate hexahydrate), Aldrich (deuterium oxide, 99.9 at. % D, and sodium dithionite), and Cambridge Isotope Laboratories (d_3-glycerol, 98 at. % D). Deuterated buffer was degassed with 99.9% pure argon; d_3-glycerol was degassed by heating under vacuum overnight followed by at least 10 freeze−pump−thaw cycles at 10^{-3} Torr. Protein samples were degassed by being rapidly purged with at least 10 vacuum/argon cycles; solid ferrous ammonium sulfate was pumped at 10^{-3} kPa for at least 1 h. The protein samples were prepared and loaded into the sample holder in an inert atmosphere.

Human and mouse p53R2 were expressed and purified as previously reported (*26*), with slight modifications. In the last steps, the samples were purified by being passed through a hydrophobic interaction column (5 × 5 mL HiTrap phenyl HP column) and eluted when the conductivity was lower than 85 mS/cm using an Äkta purification system (Pharmacia, GE-Health). p53R2 was additionally chromatographed on an anion exchange column (prepacked 2 × 5 mL HiTrap Q HP column) equilibrated with 25 mM Tris-HCl buffer (pH 7.0) and eluted at a conductivity of ∼30 mS/cm with 25 mM Tris-HCl buffer (pH 7.0) with 0.5 M KCl. The tyrosyl:radical ratio in iron-reconstituted active p53R2 was >1 per dimer, which is the normal radical yield for R2 proteins (*4*, *26*). To fully remove all iron and radicals possibly present during reconstitution, the protein was incubated with 5 mM EDTA and hydroxyurea and the solution run through a 10 mL Sephadex G25 gel filtration column to remove all the iron and to reduce the tyrosyl radical before reconstitution with Fe(II). The resultant solution was reconcentrated, and the concentration was measured using the protein absorption peak at 280 nm. The molar extinction coefficient of murine and human p53R2 is assumed to be the same (*26*) as that for mR2 (124 000 M^{-1} cm^{-1}/dimer at 280 nm) since the difference in the calculated extinction coefficients for mR2 and the p53R2 proteins is only 2.8%. Buffer exchange was carried out by diluting the apoprotein with deuterated buffer [0.15 M Hepes (pD 7.6)] and reconcentrating to ∼2 mM by ultrafiltration [Amicon (Beverly, MA) stirred YM30 ultrafiltration cell]. This process was repeated until the percentage of D_2O was greater than 99.9% of the solvent.

The degassed apoprotein was fully reduced with 1 μL of 5 mM methyl viologen and 2 μL of 10 mM dithionite before the ferrous solution was added to fully load the iron center. A ferrous ion solution was added anaerobically to the apoprotein and incubated for 15 min. The sample was transferred to an anaerobic cuvette for CD measurements. The addition of glycerol did not noticeably alter the CD spectrum. Protein samples were prepared for MCD as they were for CD with an additional step of manually mixing the protein with 60% (v/v) glycerol-d_6 (pD 7.8) until it was homogeneous to create a suitable glass. The samples were then immediately frozen in liquid nitrogen.

CD and MCD Spectroscopy. CD studies were performed on a JASCO J200D spectropolarimeter operating with a liquid nitrogen-cooled InSb detector in the 560−2000 nm region. Low-temperature MCD and VTVH MCD data were acquired on this spectropolarimeter, modified to accommodate an Oxford Instrument SM4000 7T superconducting magnet capable of magnetic fields of up to 7.0 T and temperatures down to 1.6 K. Protein samples prepared for MCD studies were slowly inserted into the cryostat to reduce strain in the resulting optical glass.

The CD and MCD spectra were fit using a constrained nonlinear least-squares procedure to find the minimum number of ligand field transitions required to simultaneously fit both spectra. Each spectroscopic method has a different selection rule; thus, transitions can have different intensities and signs but similar energies. The bands in the MCD spectrum (1.6 K) are sharper than those in the CD spectrum (278 K).

VTVH MCD data (MCD intensity, temperature, and applied magnetic field) were fit with a non-Kramers doublet model using a simplex routine that minimizes the χ^2 value. A goodness of fit parameter (χ^2/number of float parameters) was utilized in the comparison of different fit results. The $g_{||}$ values of the ground and excited sublevels as well as the energies obtained provide information about the ground spin

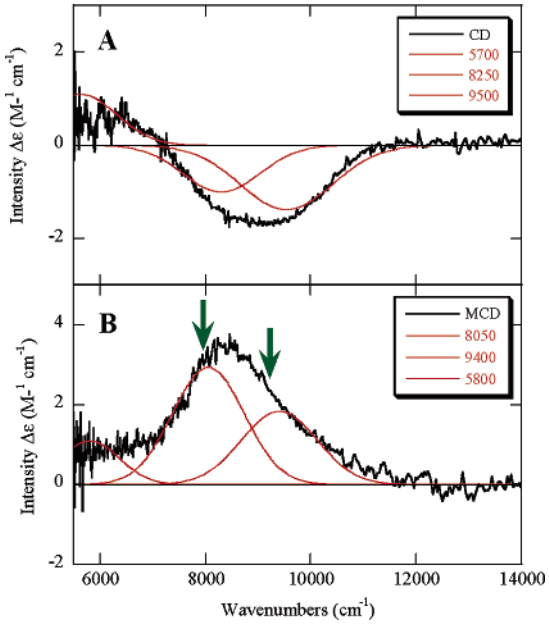

FIGURE 1: (A) CD spectrum of human p53R2, recorded at 5 °C, and (B) MCD spectrum of human p53R2, recorded at 1.6 K and 7 T. The experimental data (black line) are fit to the individual Gaussian band shapes (red line). Green arrows denote positions where VTVH data were collected (vide infra).

states and thus bridging interactions within the dimer. In addition, a spin-projection model was applied to confirm the results obtained from the doublet model and identify the specific Fe center of the dimer associated with the ligand field transition being studied by VTVH MCD. This procedure is described in the Results.

EPR Measurements. The EPR spectra were recorded at X-band on a Bruker ESP 300E or a Bruker Elexsys 500 EPR spectrometer, fitted with a Bruker ER41116DM dual-mode cavity and an Oxford ESR 900 helium flow cryostat. The ferrous p53R2 in presence of 5 mM dithionite was frozen in quartz EPR tubes after they were flushed with Ar.

RESULTS AND ANALYSIS

CD and Low-Temperature MCD Spectroscopy. NIR CD and MCD spectra for reduced human p53R2 are shown in Figure 1, with the Gaussian fit of the data shown in red. The CD spectrum (Figure 1A) is comprised of a positive transition at 5700 cm^{-1} and two negative transitions at 8250 and 9500 cm^{-1}. The MCD spectrum (Figure 1B) exhibits a small positive peak at 5800 cm^{-1} and a large broad positive peak at ~8500 cm^{-1} which can be resolved into two positive peaks at 8050 and 9400 cm^{-1}. The MCD spectra were recorded at 1.6 K and, thus, have sharper bandwidths, and the band energies shift slightly relative to the CD data recorded at 278 K. No further transitions are observed up to the protein absorbance at 280 nm. CD/MCD spectra of mouse p53R2 overlay within a standard deviation of the human p53R2 data and are shown as part A of the Supporting Information.

The three distinct peaks of hp53R2 reflect two inequivalently bound Fe(II) ions, as a single ferrous ion can give rise to only two peaks in the near-IR region. Since a six-coordinate (6C) Fe(II) would have two d → d transitions separated by ~2000 cm^{-1} around 10 000 cm^{-1}, the presence of only one transition above 8000 cm^{-1} in the CD/MCD

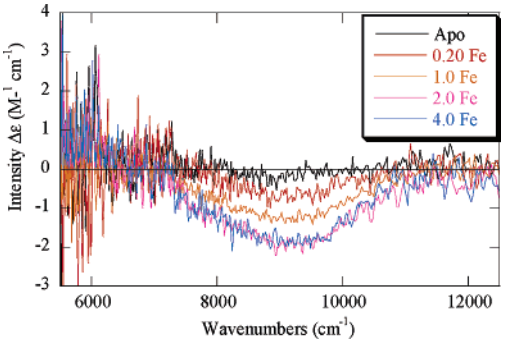

FIGURE 2: CD titration of apo human p53R2 with iron. Two equivalents of Fe is equal to a fully loaded binuclear site (i.e., 2:1 Fe:binuclear site ratio).

spectra indicates that neither iron is 6C. However, the presence of a high-energy transition in the 10 000 cm^{-1} region which is not 6C can occur only for a five-coordinate (5C) iron, as four-coordinate (4C) irons have a much lower transition energy (vide infra). A 5C square pyramidal site has two transitions, one at ~5000 cm^{-1} and a second above 10 000 cm^{-1}, while a trigonal bipyramidal 5C site has two transitions at below 10 000 and below 5000 cm^{-1}. Finally, a 4C distorted tetrahedral environment iron exhibits two low-energy LF excited transitions around 5000 cm^{-1}. In parallel to our detailed studies of *E. coli* R2, the band at 9500 cm^{-1} must be associated with a 5C iron, while the lower-energy transitions at 7800 and 5900 cm^{-1} require that the second iron be 4C.

Fe(II) CD Titrations. CD titrations were performed on apo-mR2 with ferrous ion to determine the spectral features of each metal binding site. The titration of apo-hp53R2 with ferrous iron could be measured by near-infrared CD as the Fe(II)-bound binuclear site is optically active, while unbound ferrous iron in solution is optically silent. Figure 2 shows the room-temperature CD titration of apo-hp53R2 with ferrous ion. hp53R2 has two binuclear active sites in the homodimer which can accommodate up to four iron atoms. A very broad negative transition with a maximum at ~9000 cm^{-1} and a broad weak positive transition grows in at approximately the same rate. These transitions were Gaussian resolved into three transitions (Figure 1A, red lines), and the three transitions in hp53R2 increase equally in intensity with an increase in the concentration of ferrous ions, saturating at 4 equiv of ferrous ion per homodimer (i.e., 2 equiv of iron for a binuclear site.) The binding constant (K_b) for binding of Fe(II) to hp53R2 was found to be ~$(6.4 \pm 1.0) \times 10^3$ M^{-1}. Titration experiments using the same method were conducted for mp53R2, and the K_b was found to be $(5.4 \pm 1.0) \times 10^3$ M^{-1}. This behavior, which indicates a high binding affinity, similar to that of *E. coli* R2 ($K_{b,Fe1} \sim 14.3 \pm 10^3$ M^{-1} and $K_{b,Fe2} \sim 3.3 \pm 10^3$ M^{-1}), is very different for the low-affinity cooperative binding behavior found in mR2 ($K_b \sim 0.4 \pm 10^3$ M^{-1}) (*16*, *17*). Thus, p53R2 is different in that the binuclear site binds iron equivalently (as opposed to *E. coli* R2) and with a high affinity (as opposed to mR2). Table 1 summarizes the binding constants for the four R2s.

VTVH MCD Spectroscopy. The MCD intensity of the biferrous site of hp53R2 increases as the temperature decreases, indicating that these transitions are MCD *C* term associated with a ground state which has paramagnetic doublets that are split in energy by a magnetic field.

Table 1: K_b Values for *E. coli* (*20*), Mouse (*17*), Human p53, and Mouse p53 R2

	K_b (M^{-1})
E. coli R2	$\sim(14.3 \pm 1) \times 10^3$, $\sim(3.3 \pm 1) \times 10^3$
mouse R2[a]	$\sim(0.4 \pm 1) \times 10^3$
human p53R2	$\sim(6.4 \pm 1) \times 10^3$
mouse p53R2	$\sim(5.4 \pm 1) \times 10^3$

[a] Mouse R2 at 50% saturation due to cooperativity of the binuclear site and weak Fe(II) binding.

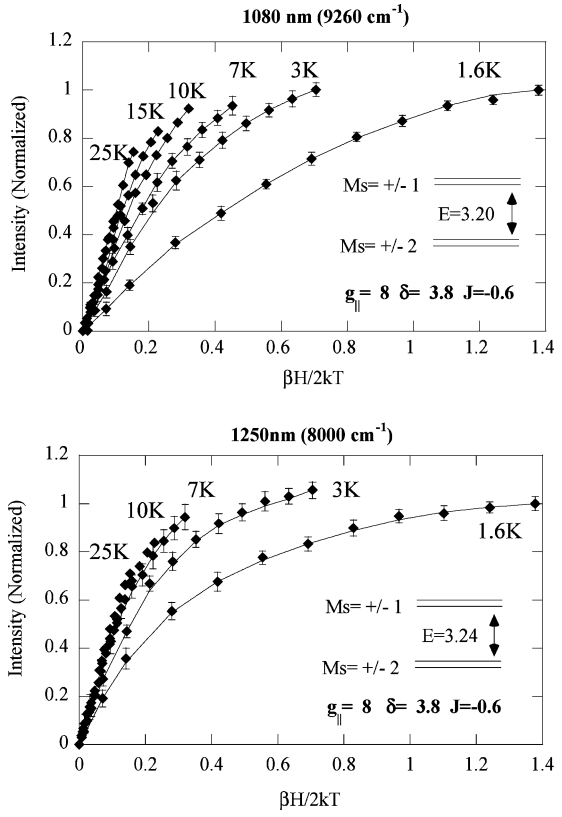

FIGURE 3: Saturation magnetization behavior of the MCD signal of human p53R2 (VTVH MCD) at 9260 (top) and 8000 cm^{-1} (bottom) with their respective doublet fits included. The intensity at one wavenumber is plotted over a range of magnetic fields (0−7 T) and temperatures (1.6−25 K) and is plotted as a function of $\beta H/2kT$, and the fit parameters are given in Table 2.

The saturation magnetization MCD curves were taken at 9,260 cm^{-1} (1080 nm) and 8000 cm^{-1} (1250 nm) (top and bottom panels of Figure 3; green arrows in Figure 1 give energy positions of the data collected). Satisfactory data could not be collected on the 5800 cm^{-1} peak due to its low signal-to-noise ratio. Both sets of VTVH MCD curves are nested, with the high-temperature data offset from the low-temperature data when the isotherms are plotted as a function of $\beta H/2kT$. This is characteristic of rhombic zero-field splitting (ZFS) of a non-Kramers doublet ground state and arises from temperature-dependent nonlinear field-induced mixing between the sublevels of the doublet. The VTVH MCD data for the two bands data do not overlay within a standard deviation for the two bands. This can be due to either different polarizations of the LF transitions on the same iron or reflect the LF transitions belonging to the two different irons of the biferrous site. Analysis of the VTVH MCD data taken at 8000 and 9260 cm^{-1} provides the ground state of the Fe_2^{II} center, which gives further insight into the Fe coordination and nature of the bridging ligands.

The VTVH MCD data were first fit using the MCD intensity expression for a non-Kramers system, allowing for the effects of a linear *B* term from field-induced mixing between states and the presence of excited sublevels of the ground state, as given by eq 1 (*46*−*48*):

$$\Delta\epsilon = \sum_i \left[(A_{\text{sat lim}})_i \left(\int_0^{\pi/2} \frac{\cos^2\theta \sin\theta}{\Gamma_i} g_{||i} \beta H \alpha_i \, d\theta - \sqrt{2} \frac{M_z}{M_{xy}} \int_0^{\pi/2} \frac{\sin^3\theta}{\Gamma_i} g_{\perp i} \beta H \alpha_i \, d\theta \right) + B_i H \gamma_i \right] \quad (1)$$

where

$$\Gamma_i = \sqrt{\delta_i^2 + (g_{||i}\beta H \cos\theta)^2 + (g_{\perp i}\beta H \sin\theta)^2}$$

$$\alpha_i = \frac{e^{-(E_i - \Gamma_i/2)/kT} - e^{-(E_i + \Gamma_i/2)/kT}}{\sum_j e^{-(E_j - \Gamma_j/2)/kT} + e^{-(E_j + \Gamma_j/2)/kT}}$$

$$\gamma_i = \frac{e^{-(E_i - \delta_i/2)/kT} + e^{-(E_i + \delta_i/2)/kT}}{\sum_j e^{-(E_j - \delta_j/2)/kT} + e^{-(E_j + \delta_j/2)/kT}}$$

where $(A_{\text{sat lim}})_i$, B_i, δ_i, $g_{||i}$, and $g_{\perp i}$ are the *C* term and *B* term MCD intensity, the rhombic ZFS, and the dimer *g* values of the *i*th doublet, respectively. E_i is the energy of the *i*th sublevel, and the energy of the ground state is defined as zero. The Boltzmann population over all states has been included in both the *C* term and the *B* term intensities as the factors α_i and γ_i, respectively. *H* is the applied magnetic field and *k* the Boltzmann constant, and M_z and M_{xy} are the transition dipole moments for the indicated directions.

The lowest-temperature (1.6 K) data collected at 9260 cm^{-1} for p53R2 were fit using eq 1 by floating A_{satlim}, *B*, δ, and $g_{||}$ while fixing $g_\perp$ and the polarization ratio M_z/M_{xy} at zero. Additional simulations where $g_\perp$ and $M_z/M_{x,y}$ were allowed to vary did not improve the fit. The best fit to the complete data set requires a single non-Kramers doublet with a $g_{||}$ of ∼8 and a δ of ∼3.8 cm^{-1}, indicating that the ground state is $M_s = \pm 2$. Fits using other values of $g_{||}$ were poor (graphically and goodness of fit). An excited doublet ∼3.2 cm^{-1} above the ground state is required to fit the higher-temperature saturation data. Inclusion of a third state does not have a significant effect on the fitting results. A good fit of eq 1 for the 8000 cm^{-1} band gives the same ground and excited state. The parameters obtained for both bands are very similar (consistent with both transitions arising from the same ground state) with variations accommodated by the A and B float parameters. These values are listed in Table 2. Included for comparison are the results for mR2 and *E. coli* R2.

A spin-Hamiltonian analysis was performed on the VTVH MCD data given above to explore the coupling between the two irons in the binuclear center. Equation 2a gives the expression for the spin Hamiltonian of a general biferrous system, which operates on the uncoupled basis set $|S_1, S_2, M_{s1}, M_{s2}\rangle$, where the subscripts indicate the two ferrous centers:

Table 2: Summary of VTVH MCD Parameters for the Ground and Excited States of the Reduced Binuclear Non-Heme Site for *E. coli* R2 (*16*, *18*), Mouse R2 (*17*), and Human p53R2 (top) and Spin-Hamiltonian Fit for the Reduced Binuclear Non-Heme *E. coli* R2, mR2, and hp53R2 from eq 2a (bottom)

	E. coli R2	mouse R2 (mp53R2)	human p53R2 (hp53R2)	
peak (cm^{-1})	7700	6250	8000	9260
$\delta 1$ (cm^{-1})	3.5	2.0	3.8	3.8
g	8.0	8.0	8.0	8.0
$\delta 2$ (cm^{-1})	10.0	1.7	3.5	3.5
g	4.0	4.0	4.0	4.0
energy (cm^{-1})	4.0	5.0	3.2	3.2
J (cm^{-1})	−0.4	$-J$ (very small)	−0.6	−0.6
D[a] (cm^{-1})	−10.0	−10.0	−10.0	−10.0
D[a] (cm^{-1})	4.0	5.0	5.0	5.0

[a] Note that combinations of either two positive or two negative D values do not give the experimental $M_s = \pm 2$ ground state. The fitting program used to obtain these D and J values cannot distinguish which iron is associated with each transition. This can be obtained from the spin projection model.

$$H = -2J\hat{S}_1\hat{S}_2 + D_1[\hat{S}_{z_1}{}^2 - 1/3S(S+1)] + E_1(\hat{S}_{x_1}{}^2 - \hat{S}_{y_1}{}^2) + D_2[\hat{S}_{z_2}{}^2 - 1/3S(S+1)] + E_2(\hat{S}_{x_2}{}^2 - \hat{S}_{y_2}{}^2) + g_{z_1}\beta H_z\hat{S}_{z_1} + g_{x_1}\beta H_x\hat{S}_{x_1} + g_{y_1}\beta H_y\hat{S}_{y_1} + g_{z_2}\beta H_z\hat{S}_{z_2} + g_{x_2}\beta H_x\hat{S}_{x_2} + g_{y_2}\beta H_y\hat{S}_{y_2} \quad (2a)$$

where J is the exchange coupling between the two irons, D_1, D_2, E_1, and E_2 are the axial and rhombic ZFS parameters, and H is the magnetic field. Zeeman terms ($g_{z_1}\beta H_{z_1}S_{z_1}$ ... etc.) are also included, where the g value can be coupled to the ZFS parameters using ligand field theory as given in eqs 2b and 2c. λ is the Fe(II) ground state spin-orbit coupling constant ($\sim$100 cm^{-1}), and k^2 is the Stevens orbital reduction factor (i.e., $|k| < 1$) and accounts for the effects of covalency.

$$D_{Fe^{2+}} = \frac{-k^2\lambda}{4}(g_{xFe^{2+}} + g_{yFe^{2+}} - 2g_{zFe^{2+}}) \quad (2b)$$

$$E_{Fe^{2+}} = \frac{-k^2\lambda}{4}(g_{yFe^{2+}} - g_{xFe^{2+}}) \quad (2c)$$

A high-spin ferrous ion has an $S = 2$ ground state with $M_s = 0$, ± 1, and ± 2. This 5-fold degeneracy will split due to zero-field splitting. In an exchange-coupled system, the two ferrous ions can also interact through bridging ligands to give $S_{tot} = |S_1 + S_2|$ ... $|S_1 - S_2| = 4$, 3, 2, 1, and 0 levels. These levels are split by the exchange coupling $H = -2JS_1S_2$ to generate $(2S_{tot} + 1)M_s$ degenerate levels, which are further split in energy by the zero-field splitting (ZFS). Since the magnitudes of D and J are comparable in binuclear non-heme ferrous systems, their combined effects need to be considered.

A 25 × 25 matrix describing the interaction of the M_s sublevels with each other as functions of J and D is generated, and diagonalization of this matrix in zero magnetic field gives the wave functions of the binuclear ferrous spin states and their energies. These are dependent on the relative magnitudes and signs of the exchange coupling and the ZFS. The magnitude of the D values are constrained to be less than |15| cm^{-1} (the largest value observed in model systems and ligand field calculations); the maximum $|E/D|$ is $^1/_3$ by definition. The fits using the results obtained from the doublet model are summarized in the bottom of Table 2. From Table 2, hp53R2 has a ground state with $M_s = \pm 2$ ($g = 8$) and a lowest excited state of a doublet with an $M_s = \pm 1$ ($g = 4$). This situation occurs when the two D values have opposite signs and J is negative. The J value for hp53R2 is -0.6 ± 0.1 cm^{-1}, indicating an antiferromagnetically coupled system. Part B of the Supporting Information gives a condensed correlation diagram of the energy levels of the binuclear ferrous ground state with a D_1 of -10 cm^{-1} and a D_2 of 5 cm^{-1} with the positions of mR2, *E. coli* R2, and hp53R2 shown.

In the analysis of the VTVH MCD data for hp53R2 given above, second-order Zeeman contributions have been incorporated via the inclusion of the empirical B term in the MCD intensity expression (B_i in eq 1). These empirical float parameters are used to account for the field-induced mixing between sublevels of the ground state. The data can also be fit directly with the spin-Hamiltonian wave functions and the fact that the MCD intensity is proportional to the spin-expectation values of the single iron center being studied by MCD projected onto the dimer states. This complementary fitting approach uses the parameters D_1, E_1, D_2, E_2, and J and the effective transition moment products M_{xy}, M_{xz}, and M_{yz} to obtain the best fit. In this approach, D_1 is the Fe(II) center associated with the d → d transition studied by VTVH MCD. Thus, through correlation of D_1 with VTVH MCD data for a specific LF transition, it is sometimes possible to identify which of the irons in the binuclear site is associated with the MCD transition being studied. This has been carried out in previous studies, and details of the simulation program are given in ref *16*. The best spin-Hamiltonian fit to the VTVH MCD data taken at 9260 cm^{-1} is shown in Figure 4A. The data were best fit with a D_1 of -9.26 cm^{-1} and a D_2 of 5.8 cm^{-1} with a negative J value of -0.6 cm^{-1}. A good fit could not be obtained with a positive D_1 value; thus, the transition at 9260 cm^{-1} could be associated with only the 5C iron.

Initially, a variety of VTVH MCD simulations were performed to map out the solution space for the 8000 cm^{-1} saturation magnetization data in Figure 3. The data could only be reasonably fit with either a combination of two negative D values of different magnitudes or a postive and negative D for the two ferrous centers (Figure 4B). However, from the doublet fitting, we were able to eliminate the former option as a local minimum. The final fit for the 8000 cm^{-1} peak was a D_1 of 5.6 cm^{-1} and a D_2 of -10 cm^{-1} with a negative J value of -0.6 cm^{-1}. Thus, the 8000 cm^{-1} band reflects a 4C iron since this Fe(II) center has a positive ZFS.

The J and D values which result from the VTVH MCD data fit with the spin-Hamiltonian method are consistent with these obtained from the doublet fitting method and the band assignments made in the previous section. Table 3 presents the spin-Hamiltonian fits for the three R2 systems. Note that these fits using the method described above were not sensitive to the rhombicity of the Fe(II) site. However, the fits using the doublet model (eq 1) require an E/D of >0 for each Fe(II), as the non-Kramers doublets exhibit significant splitting.

Integer Spin EPR Studies. Biferrous mR2 has a strong integer spin X-band EPR signal in ≥20% glycerol with a g_{obs} around 12 (*49*) that can be observed in both perpendicular

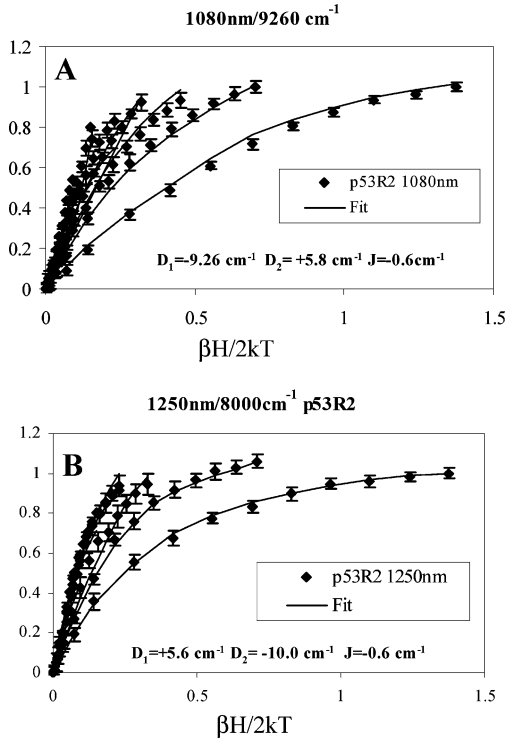

FIGURE 4: Spin-Hamiltonian fits using the spin projection model of the p53R2 VTVH MCD data taken at (A) 1080 nm (9260 cm^{-1}) and (B) 1250 nm (8000 cm^{-1}). Parameters are summarized in Table 3.

and parallel mode X-band EPR spectra in the temperature range of 4−10 K. hp53R2 and mp53R2 do not have any detectable X-band integer spin EPR signal in perpendicular and parallel mode (data not shown), as observed for *E. coli* R2.

In summary, from the analysis of the CD, MCD, and VTVH data, the reduced form of hp53R2 contains a 4C,5C diiron center, with peaks at 5700, 8400, and 9500 cm^{-1}. The peak at 9500 cm^{-1} is associated with the 5C Fe(II), and the 5700 cm^{-1} and 8400 cm^{-1} transitions are associated with the 4C Fe(II). The complex has a weak antiferromagnetic coupling J value of -0.6 cm^{-1} indicating the presence of μ-1,3-carboxylate bridges.

DISCUSSION

The ability of both hp53R2 and mp53R2 to generate a tyrosine radical with EPR properties similar to those of mR2 and *E. coli* R2 indicated its potential as a class I ribonucleotide reductase with a similar binuclear iron site. The CD/MCD/VTVH MCD spectroscopic studies on the reduced hp53R2 and mp53R2 presented here reveal that the overall structure of the biferrous site of mammalian p53R2 bears a strong resemblance to the structures of other members of the R2 family (*16*, *17*). The hp53R2 and mp53R2 X-band tyrosyl radicals are also very similar to the mR2 radical (*26*, *50*). This is not surprising since the active form of p53R2 binds and performs turnovers with the same RNR R1 subunit used by normal R2. Figure 5 shows the CD (A) and MCD (B) spectra of hp53R2 overlaid with those of R2 from *E. coli* and mouse. All three exhibit the spectroscopic features of a 4C,5C biferrous center. Analysis of the VTVH MCD data in Figure 3 indicates that hp53R2 has a non-Kramers doublet ground state ($M_s = \pm 2$) with the ferrous ions antiferromagnetically coupled ($J = -0.6$ cm^{-1}). Previous studies concluded that binuclear ferrous sites with weak antiferromagnetism arise from carboxylate bridges providing a poor superexchange pathway for electron transfer. Complexes with both carboxylates bridged in a μ-1,3 fashion exhibit a similar weak antiferromagnetic interaction (*51*). The ground state of hp53R2 further reflects one Fe(II) with a positive small D and the second Fe(II) with a larger negative D. This also mirrors the results of the R2 family, further defining a model where one iron is 4C (positive D) and the other iron is 5C (negative D).

While the spectroscopic similarity of hp53R2 and mp53R2 to the R2 family was anticipated, from Figure 5B, the intensity pattern of both mammalian p53R2s in MCD bears a greater similarity to that of *E. coli* R2 than to that of mR2. In addition, the ground state parameters of hp53R2 from Table 2 more closely resemble those of *E. coli* R2, with a larger J (ca. -0.5 cm^{-1}) and δ ($\sim$3.8 cm^{-1}) in comparison to those of mR2 ($J \sim 0$, $\delta \sim 2.0$ cm^{-1}). This is consistent with the absence of an X-band integer spin EPR signal for both mammalian p53R2s and *E. coli* R2, while reduced mR2 exhibits an integer EPR signal which reflects its smaller δ. This greater similarity to *E. coli* R2 shown by human and mouse p53R2 is interesting, considering the homology between mR2 and human and mouse p53R2. While the CD/MCD data of human and mouse p53R2 are similar with those of the other R2 families, the CD sign in human and mouse p53R2 ($\sim$7000−8000 cm^{-1}) is negative. This indicates that there is a conformational difference in the vicinity of this iron center, although the iron remains 4C. In addition, the sign of the highest-energy peak ($\sim$9500 cm^{-1}) in the MCD spectrum of human and mouse p53R2 is positive, in comparison to those of *E. coli* and mouse R2, which have a negative sign for this transition. This indicates a perturbation in the electronic structure of the 5C iron center. It should be noted that while the CD and MCD signs of mR2 and *E. coli* R2 are the same, the middle transition ($\sim$7000 cm^{-1}) of mR2 is 300−600 cm^{-1} lower in energy. Table 4 gives the transitions and signs of human and mouse p53R2 and compares these to the equivalent transitions of *E. coli* R2 and mouse (mammalian) R2.

Prior studies of mononuclear ferrous systems showed that MCD d → d transitions are often both positive, which is a deviation from the sum rule (equal in magnitude but opposite in sign). This all-positive MCD spectrum arises from the removal of the orbital degeneracy of the ground state and introduction of spin orbit coupling (SOC) between its rhombically split components. Since there is no matrix element of the orbital angular momentum, L, between the components of the excited state levels, they cannot directly spin orbit couple. This would preclude the MCD intensity which arises from the pseudo-A mechanism (*52*). In *E. coli* R2 and mR2, the negative MCD transition in Figure 5 reflects a distortion of the ligand field in the 5C iron which would allow mixing between the d_π and d_σ orbitals. This provides a mechanism for SOC between the excited states (*53*). A positive peak in the MCD spectrum of p53R2 in the higher-energy band in Figure 1 indicates that the 5C center is more axial than in *E. coli* R2 or mR2. In addition to the sign differences, the middle transition in p53R2 ($\sim$8250−8400 cm^{-1}) has significantly shifted to higher energy in comparison to the R2s previously studied. This shift to higher energy

Table 3: Summary of Spin-Hamiltonian Parameters for Reduced Binuclear Non-Heme *E. coli* R2 (*17*), Mouse R2 (*17*), and hp53R2

	E. coli R2 at 7700 cm^{-1}	mouse R2 at 6250 cm^{-1}	hp53R2 at 8000 cm^{-1}	hp53R2 at 9260 cm^{-1}
J (cm^{-1})	$-0.65 < J < -0.3$	$-0.5 < J < 0.5$	$-0.6 < J < -0.54$	$-0.6 < J < -0.54$
D_1[a] (cm^{-1})	$3 < D < 9$	$8 < D < 10$	$4 < D < 6$	$-11 < D < -9$
D_2 (cm^{-1})	$-11 < D < -7$	$-15 < D < -10$	$-11 < D < -8$	$4 < D < 6$

[a] D_1 is assigned to the Fe(II) center associated with the d → d transition studied by VTVH MCD. In this case, D_1 (8000 cm^{-1}) is 4C Fe and D_1 (9260 cm^{-1}) is 5C Fe.

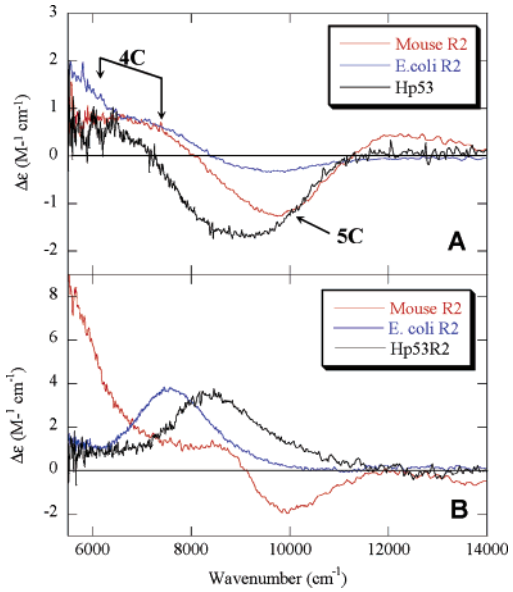

FIGURE 5: (A) CD spectra of human p53R2 (black), *E. coli* R2 (blue), and mR2 (red) recorded at 5 °C and (B) MCD spectra of human p53R2 (black), *E. coli* R2 (blue), and mR2 (red) recorded at 1.6 K and 7 T.

Table 4: Signs and Peak Positions of *E. coli* R2, Mouse R2, p53R2, and Mouse p53R2

	E. coli R2	mR2	hp53R2	mp53R2
CD (cm^{-1})	5500 (+)	5600 (+)	5700 (+)	5700 (+)
	7000 (+)	6700 (+)	8250 (−)	8250 (−)
	9700 (−)	9600 (−)	9500 (−)	9500 (−)
MCD (cm^{-1})	5200 (+)	5500 (+)	5800 (+)	5800 (+)
	7400 (+)	6800 (+)	8050 (+)	8050 (+)
	9100 (−)[a]	10000 (−)	9400 (+)	9400 (+)

[a] The peak at 9100 cm^{-1} is seen at a low Fe(II) concentration.

indicates the 4C iron is more distorted away from a tetrahedral geometry.

There are a number of possible small structural distortions that can cause these spectral changes, including a shift of a bridging carboxylate and distortion of the axial ligand on one Fe(II) center. Crystal structures of mR2 have been determined and indicate that mR2 has a more labile iron center as well as a more open structure than *E. coli* R2 (*25, 54*). Comparison of the J values of the three R2s (Table 2) indicates that p53R2 of both human and mouse are closer to *E. coli* R2 than mR2. Recently determined crystal structures have shown that the Fe(II)−Fe(II) distance is longer for *E. coli* R2 than for mR2 (*25*). Both the dithionite-reduced and Fe(II)-soaked *E. coli* R2 have an Fe(II)−Fe(II) distance of 3.9−3.6 Å, while the Fe(II)-soaked mR2 iron−iron distance was 3.4 Å. Examination of the crystal structure of mouse and *E. coli* R2 shows that one of the bridging carboxylates (E267) was shifted more toward the 5C iron in a more bidentate fashion in mR2. The carboxylate (E238 in *E. coli* R2) which bridges the two irons in *E. coli* R2 is more centered between the two irons of the biferrous site in mR2.

Finally, the main difference between p53R2 and mR2 is in the mode and ability to bind iron. The free radical iron center in mR2 is more labile, losing 50% of its iron after 30 min at 37 °C (*44, 45*). Although hp53R2 is most homologous with mammalian (mouse) R2, its binding constant for ferrous iron is more similar to that of *E. coli* R2. In addition, p53R2 lacks the cooperative Fe(II) binding found in mR2 (*7, 17, 54*). Four crystal structures of mR2 at pH 6 (and lower) soaked with iron(II) under different aerobic reducing conditions exhibit significant carboxylate shifts (*7, 24*). The CD/MCD spectra of mR2 at pD 7.9 (pH 7.5) in 50 mM HEPES and 100 mM KCl buffer exhibited only one species but confirmed the lower affinity for iron in titration experiments. The fact that p53R2 binds Fe(II) quite readily as opposed to mR2 may reflect a regulatory mechanism in mammalian R2 which prevents formation of excess tyrosyl radicals or other harmful reactive species in a resting, undamaged cell. As p53R2 is triggered only during DNA repair, regulation by ferrous ion may be unnecessary. This difference in ferrous iron affinity between mammalian p53R2 and mR2 could be exploited for the therapeutic inhibition of R2 during rapid cell division, e.g., the growth cycle of certain cancer cells, with the use of Fe(II) chelators.

In summary, this study presents detailed electronic and geometric structural insight into the active site of the p53R2 enzyme. The spectroscopic methodology shows that the biferrous center for p53R2 consists of one five- and one four-coordinate iron which are weakly antiferromagnetically coupled through μ-1,3 bridging carboxylates. The active site structure obtained for the reduced form of p53R2 has been correlated to those of *E. coli* R2 and mR2. These species have a common structure for the dioxygen reactive forms of R2; however, they differ in iron binding ability, which may relate to regulation and function.

ACKNOWLEDGMENT

We thank Professor Lars Thelander (University of Umeå, Umeå, Sweden) for generously providing the *E. coli* strains overproducing mR2, mouse p53R2, and human p53R2.

SUPPORTING INFORMATION AVAILABLE

CD and MCD spectra of mp53R2 (part A) and a condensed correlation diagram of the energy levels of the binuclear ferrous ground state with a D_1 of 5 cm^{-1} and a D_2 of -10 cm^{-1} with the positions of mouse R2 (green), *E. coli* R2 (black), and p53R2 (red) given (part B). This material is available free of charge via the Internet at http://pubs.acs.org.

REFERENCES

1. Eklund, H., Uhlin, U., Farnegardh, M., Logan, D. T., and Nordlund, P. (2001) Structure and function of the radical enzyme ribonucleotide reductase, *Prog. Biophys. Mol. Biol. 77*, 177−268.

2. Thelander, L., and Reichard, P. (1979) Reduction of ribonucleotides, *Annu. Rev. Biochem. 48*, 133−158.
3. Nordlund, P., and Eklund, H. (1995) Di-iron-carboxylate proteins, *Curr. Opin. Struct. Biol. 5*, 758−766.
4. Nordlund, P., and Reichard, P. (2006) Ribonucleotide reductases, *Annu. Rev. Biochem. 75*, 681−706.
5. Bollinger, J. M., Jr., Edmondson, D. E., Huynh, B. H., Filley, J., Norton, J. R., and Stubbe, J. (1991) Mechanism of assembly of the tyrosyl radical radical-dinuclear iron cluster cofactor of the ribonucleotide reductase, *Science 253*, 292−298.
6. Stubbe, J., Nocera, D. G., Yee, C. S., and Chang, M. C. (2003) Radical Initiation in the Class I Ribonucleotide Reductase: Long-Range Proton-Coupled Electron Transfer? *Chem. Rev. 103*, 2167−2201.
7. Kolberg, M., Strand, K. R., Graff, P., and Andersson, K. K. (2004) Structure, function, and mechanism of ribonucleotide reductases, *Biochim. Biophys. Acta 1699*, 1−34.
8. Sjoberg, B. M. (1997) Ribonucleotide reductases: A group of enzymes with different metallosites and a similar reaction mechanism, *Struct. Bonding 88*, 139−173.
9. Andersson, K. K., and Graslund, A. (1995) Diiron-oxygen proteins, *Adv. Inorg. Chem. 43*, 359−408.
10. Stubbe, J. A., and van derk Donk, W. A. (1998) Protein Radicals in Enzyme Catalysis, *Chem. Rev. 98*, 705−762.
11. Reichard, P. (1993) From RNA to DNA, why so many ribonucleotide reductases? *Science 260*, 1773−1777.
12. Jordan, A., and Reichard, P. (1998) Ribonucleotide Reductases, *Annu. Rev. Biochem. 67*, 71−98.
13. Nordlund, P., and Eklund, H. (1993) Structure and function of the *Escherichia coli* ribonucleotide reductase protein R2, *J. Mol. Biol. 232*, 123−164.
14. Hogbom, M., Stenmark, P., Voevodskaya, N., McClarty, G., Graslund, A., and Nordlund, P. (2004) The Radical Site in Chlamydial Ribonucleotide Reductase Defines a New R2 Subclass, *Science 305*, 245−248.
15. Moenne-Loccoz, P., Baldwin, J., Ley, B. A., Loehr, T. M., and Bollinger, J. M., Jr. (1998) O_2 Activation by Non-Heme Diiron Proteins: Identification of a Symmetric μ-1,2-Peroxide in a Mutant of Ribonucleotide Reductase, *Biochemistry 37*, 14659−14663.
16. Yang, Y. S., Baldwin, J., Ley, B. A., Bollinger, J. M., Jr., and Solomon, E. I. (2000) Spectroscopic and Electronic Structure Description of the Reduced Binuclear Non-Heme Iron Active Site in Ribonucleotide Reductase from *E. coli*: Comparison to Reduced Δ^9 Desaturase and Electronic Structure Contributions to Differences in O_2 Reactivity, *J. Am. Chem. Soc. 122*, 8495−8510.
17. Strand, K. R., Yang, Y. S., Andersson, K. K., and Solomon, E. I. (2003) Circular Dichroism and Magnetic Circular Dichroism Studies of the Biferrous Form of the R2 Subunit of Ribonucleotide Reductase from Mouse: Comparison to the R2 from *Escherichia coli* and Other Binuclear Ferrous Enzymes, *Biochemistry 42*, 12223−12234.
18. Pulver, S. C., Tong, W. H., Bollinger, J. M., Jr., Stubbe, J., and Solomon, E. I. (1995) Circular Dichroism and Magnetic Circular Dichroism Studies of the Fully Reduced Binuclear Non-Heme Iron Active Site in the *Escherichia coli* R2 Subunit of Ribonucleoside Diphosphate Reductase, *J. Am. Chem. Soc. 117*, 12664−12678.
19. Solomon, E. I., Brunold, T. C., Davis, M. I., Kemsley, J. N., Lee, S. K., Lehnert, N., Neese, F., Skulan, A. J., Yang, Y. S., and Zhou, J. (2000) Geometric and Electronic Structure/Function Correlations in Non-Heme Iron Enzymes, *Chem. Rev. 100*, 235−349.
20. Thelander, L., and Graslund, A. (1994) Ribonucleotide Reductase in Mammalian Systems, *Met. Ions Biol. Syst. 30*, 109−129.
21. Logan, D. T., Su, X.-D., Åberg, A., Regnström, K., Hajdu, J., Eklund, H., and Nordlund, P. (1996) Crystal structure of reduced protein R2 of ribonucleotide reductase: The structural basis for oxygen activation at a dinuclear iron site, *Structure 4*, 1053−1064.
22. Voegtli, W. C., Khidekel, N., Baldwin, J., Ley, B. A., Bollinger, J. M., Jr., and Rosenzweig, A. C. (2000) Crystal Structure of the Ribonucleotide Reductase R2 Mutant that Accumulates a μ-1,2-Peroxodiiron(III) Intermediate during Oxygen Activation, *J. Am. Chem. Soc. 122*, 3255−3261.
23. Sommerhalter, M., Saleh, L., Bollinger, J. M., Jr., and Rosenzweig, A. C. (2005) Structure of *Escherichia coli* ribonucleotide reductase R2 in space group P6122, *Acta Crystallogr. D61*, 1649−1654.
24. Strand, K. R., Karlsen, S., Kolberg, M., Røhr, Å. K., Görbitz, C. H., and Andersson, K. K. (2004) Crystal Structural Studies of Changes in the Native Dinuclear Iron Center of Ribonucleotide Reductase Protein R2 from Mouse, *J. Biol. Chem. 279*, 46794−46801.
25. Tanaka, H., Arakawa, H., Yamaguchi, T., Shiraishi, K., Fukuda, S., Matsui, K., Takei, Y., and Nakamura, Y. (2000) A ribonucleotide reductase gene involved in a p53-dependent cell-cycle checkpoint for DNA damage, *Nature 404*, 42−49.
26. Guittet, O., Håkansson, P., Voevodskaya, N., Fridd, S., Gräslund, A., Arakawa, H., Nakamura, Y., and Thelander, L. (2001) Mammalian p53R2 Protein Forms an Active Ribonucleotide Reductase in Vitro with the R1 Protein, Which Is Expressed Both in Resting Cells in Response to DNA Damage and in Proliferating Cells, *J. Biol. Chem. 276*, 40647−40652.
27. Levine, A. J. (1997) p53, the cellular gatekeeper for growth and division, *Cell 88*, 323−331.
28. Chang, C., Simmons, D. T., Martin, M. A., and Mora, P. T. (1979) Identification and partial characterization of new antigens from simian virus 40-transformed mouse cells, *J. Virol. 31*, 463−471.
29. Kress, M., May, E., Cassingena, R., and May, P. (1979) Simian virus 40-transformed cells express new species of proteins precipitable by anti-simian virus 40 tumor serum, *J. Virol. 31*, 472−483.
30. Lane, D. P., and Crawford, L. V. (1979) T antigen is bound to a host protein in SV40-transformed cells, *Nature 278*, 261−263.
31. Kimura, T., Takeda, S., Sagiya, Y., Gotoh, M., Nakamura, Y., and Arakawa, H. (2003) Impaired function of p53R2 in Rrm2b-null mice causes severe renal failure through attenuation of dNTP pools, *Nat. Genet. 34*, 440−445.
32. Powell, D. R., Desai, U., Sparks, M. J., Hansen, G., Gay, J., Schrick, J., Shi, Z., Hicks, J., and Vogel, P. (2005) Rapid development of glomerular injury and renal failure in mice lacking p53R2, *Pediatr. Nephrol. 20*, 432−440.
33. Shan, B., Xu, J., Zhou, Y., Morris, C. A., and Morris, G. F. (2003) Induction of p53-dependent Activation of the Human Proliferating Cell Nuclear Antigen Gene in Chromatin by Ionizing Radiation, *J. Biol. Chem. 278*, 44009−44017.
34. Zhou, B. B. S., and Elledge, S. J. (2000) The DNA damage response: Putting checkpoints in perspective, *Nature 408*, 433−439.
35. Yamaguchi, T., Matsuda, K., Sagiya, Y., Iwadate, M., Fujino, M. A., Nakamura, Y., and Arakawa, H. (2001) p53R2-dependent Pathway for DNA Synthesis in a p53-regulated Cell Cycle Checkpoint1, *Cancer Res. 61*, 8256−8262.
36. Zhou, B., Shao, J., Su, L., Yuan, Y.-C., Qi, C., Shih, J., Xi, B., Chu, B., and Yen, Y. (2005) A dityrosyl-diiron radical cofactor center is essential for human ribonucleotide reductases, *Mol. Cancer Ther. 4*, 1830−1836.
37. Hakansson, P., Hofer, A., and Thelander, L. (2006) Regulation of mammalian ribonucleotide reduction and dNTP pools after DNA damage and in resting cells, *J. Biol. Chem. 281*, 7834−7841.
38. Graff, P., Seim, J., Åmellem, Ø., Arakawa, H., Nakamura, Y., Andersson, K. K., Stokke, T., and Pettersen, E. O. (2004) Counteraction of pRb-dependent protection after extreme hypoxia by elevated ribonucleotide reductase, *Cell Proliferation 37*, 367−383.
39. Kashlan, O. B., and Cooperman, B. S. (2003) Comprehensive model for allosteric regulation of mammalian ribonucleotide reductase: Refinements and consequences, *Biochemistry 42*, 1696−1706.
40. Kashlan, O. B., Scott, C. P., Lear, J. D., and Cooperman, B. S. (2002) Comprehensive Model for the Allosteric Regulation of Mammalian Ribonucleotide Reductase. Functional Consequences of ATP- and dATP-Induced Oligomerization of the Large Subunit, *Biochemistry 41*, 462−474.
41. Cooperman, B. S., and Kashlan, O. B. (2003) A comprehensive model for the allosteric regulation of class Ia ribonucleotide reductases, *Adv. Enzyme Regul. 43*, 167−182.
42. Chabes, A. L., Bjorklund, S., and Thelander, L. (2004) S phase-specific transcription of the mouse ribonucleotide reductase R2 gene requires both a proximal repressive E2F-binding site and an upstream promoter activating region, *J. Biol. Chem. 279*, 10796−10807.
43. Mann, G. J., Graslund, A., Ochiai, E. I., Ingemarson, R., and Thelander, L. (1991) Purification and characterization of recombinant mouse and herpes simplex virus ribonucleotide reductase R2 subunit, *Biochemistry 30*, 1939−1947.
44. Nyholm, S., Mann, G. J., Johansson, A. G., Bergeron, R. J., Graslund, A., and Thelander, L. (1993) Role of ribonucleotide

reductase in inhibition of mammalian cell growth by potent iron chelators, *J. Biol. Chem. 268*, 26200−26205.
45. Solomon, E. I., Pavel, E. G., Loeb, K. E., and Campochiaro, C. (1995) Magnetic circular dichroism spectroscopy as a probe of the geometric and electronic structure of non-heme ferrous enzymes, *Coord. Chem. Rev. 144*, 369−460.
46. Stevens, P. J. (1974) Magnetic circular dichroism, *Annu. Rev. Phys. Chem. 25*, 201−203.
47. Zhang, Y., Gebhard, M. S., and Solomon, E. I. (1991) Spectroscopic studies of the non-heme ferric active site in soybean lipoxygenase: Magnetic circular dichroism as a probe of electronic and geometric structure. Ligand-field origin of zero-field splitting, *J. Am. Chem. Soc. 113*, 5162−5175.
48. Bennet, D. E., and Johnson, M. K. (1987) The electronic and magnetic properties of rubredoxin: A low-temperature magnetic circular dichroism study, *Biochim. Biophys. Acta 911*, 71−80.
49. Atta, M., Debaecker, N., Andersson, K. K., Latour, J.-M., Thelander, L., and Gräslund, A. (1996) EPR and multi-field magnetization of reduced forms of the binuclear iron center in ribonucleotide reductase from mouse, *J. Biol. Inorg. Chem. 1*, 210−220.
50. Graff, P., Åmellen, Ø., Andersson, K. K., and Pettersen, E. O. (2002) Role of ribonucleotide reductase in regulation of cell cycle progression during and after exposure to moderate hypoxia, *Anticancer Res. 22*, 59−68.
51. Wei, P.-p., Skulan, A. J., Wade, H., DeGrado, W. F., and Solomon, E. I. (2005) Spectroscopic and Computational Studies of the de Novo Designed Protein DF2t: Correlation to the Biferrous Active Site of Ribonucleotide Reductase and Factors That Affect O2 Reactivity, *J. Am. Chem. Soc. 127*, 16098−16106.
52. Pavel, E. G., Kitajima, N., and Solomon, E. I. (1998) Magnetic Circular Dichroism Spectroscopic Studies of Mononuclear Non-Heme Ferrous Model Complexes. Correlation of Excited- and Ground-State Electronic Structure with Geometry, *J. Am. Chem. Soc. 120*, 3949−3962.
53. Davis, M. I., Wasinger, E. C., Decker, A., Pau, M. Y. M., Vaillancourt, F. H., Bolin, J. T., Eltis, L. D., Hedman, B., Hodgson, K. O., and Solomon, E. I. (2003) Spectroscopic and Electronic Structure Studies of 2,3-Dihydroxybiphenyl 1,2-Dioxygenase: O_2 Reactivity of the Non-Heme Ferrous Site in Extradiol Dioxygenases, *J. Am. Chem. Soc. 125*, 11214−11227.
54. Strand, K. R., Karlsen, S., and Andersson, K. K. (2002) Cobalt Substitution of Mouse R2 Ribonucleotide Reductase as a Model for the Reactive Diferrous State, *J. Biol. Chem. 277*, 34229−34238.

BI061127P